

High-quality ghost imaging based on undersampled natural-order Hadamard source

Kang Liu(刘炕), Cheng Zhou(周成), Jipeng Huang(黄继鹏), Hongwu Qin(秦宏伍), Xuan Liu(刘轩), Xinwei Li(李鑫伟), and Lijun Song(宋立军)

Citation: Chin. Phys. B, 2024, 33 (**9**): 094204. DOI: 10.1088/1674-1056/ad62e1
Journal homepage: http://cpb.iphy.ac.cn; http://iopscience.iop.org/cpb

What follows is a list of articles you may be interested in

High-visibility ghost imaging with phase-controlled discrete classical light sources

Xueying Wu(仵雪滢), Yue Zhao(赵岳), and Liming Li(李利明)
Chin. Phys. B, 2024, 33 (**7**): 074202. DOI: 10.1088/1674-1056/ad4631

Optical encryption scheme based on spread spectrum ghost imaging

Jin-Fen Liu(刘进芬), Yue Dong(董玥), Le Wang(王乐), and Sheng-Mei Zhao(赵生妹)
Chin. Phys. B, 2023, 32 (**7**): 074202. DOI: 10.1088/1674-1056/acbf27

Principle of subtraction ghost imaging in scattering medium

Qin Fu(付芹), Yanfeng Bai(白艳锋), Wei Tan(谭威), Xianwei Huang(黄贤伟), Suqin Nan(南苏琴), and Xiquan Fu(傅喜泉)
Chin. Phys. B, 2023, 32 (**6**): 064203. DOI: 10.1088/1674-1056/acb202

probability theory for filtered ghost imaging

Zhong-Yuan Liu(刘忠源), Shao-Ying Meng(孟少英), and Xi-Hao Chen(陈希浩)
Chin. Phys. B, 2023, 32 (**4**): 044204. DOI: 10.1088/1674-1056/ac981e

Ghost imaging based on the control of light source bandwidth

Zhao-Qi Liu(刘兆骐), Yan-Feng Bai(白艳锋), Xuan-Peng-Fan Zou(邹璇彭凡), Li-Yu Zhou(周立宇), Qin Fu(付芹), and Xi-Quan Fu(傅喜泉)
Chin. Phys. B, 2023, 32 (**3**): 034210. DOI: 10.1088/1674-1056/ac6edd

---

High-quality ghost imaging based on undersampled natural-order Hadamard source

Kang Liu(刘炕)[1], Cheng Zhou(周成)[2,†], Jipeng Huang(黄继鹏)[2], Hongwu Qin(秦宏伍)[1,‡], Xuan Liu(刘轩)[3], Xinwei Li(李鑫伟)[4], and Lijun Song(宋立军)[5,§]

[1] *School of Electronic Information Engineering, Changchun University, Changchun* 130022, *China*
[2] *School of Physics, Northeast Normal University, Changchun* 130024, *China*
[3] *College of Electronic and Information Engineering, Changchun University of Science and Technology, Changchun* 130022, *China*
[4] *Jilin Engineering Laboratory for Quantum Information Technology, Jilin Engineering Normal University, Changchun* 130052, *China*
[5] *Changchun Institute of Technology, Changchun* 130012, *China*

(Received 22 May 2024; revised manuscript received 12 July 2024; accepted manuscript online 15 July 2024)

Improving the speed of ghost imaging is one of the main ways to leverage its advantages in sensitivity and imperfect spectral regions for practical applications. Because of the proportional relationship between image resolution and measurement time, when the image pixels are large, the measurement time increases, making it difficult to achieve real-time imaging. Therefore, a high-quality ghost imaging method based on undersampled natural-order Hadamard is proposed. This method uses the characteristics of the Hadamard matrix under undersampling conditions where image information can be fully obtained but overlaps, as well as deep learning to extract aliasing information from the overlapping results to obtain the true original image information. We conducted numerical simulations and experimental tests on binary and grayscale objects under undersampling conditions to demonstrate the effectiveness and scalability of this method. This method can significantly reduce the number of measurements required to obtain high-quality image information and advance application promotion.

Keywords: ghost imaging, natural-order Hadamard, deep learning

PACS: 42.30.–d, 42.30.Va, 42.30.Wb **DOI:** 10.1088/1674-1056/ad62e1

1. Introduction

Ghost imaging (GI) is a new imaging method that obtains image information through computation. Its unique means of information acquisition is the single-pixel detection of the overall information of an object encoded by a series of light fields.[1–3] Consequently, a succession of single-pixel detectors measure signals, which incurs considerable time consumption and thereby limits the imaging speed of large image resolutions. Although GI has certain advantages over traditional point-to-point optical imaging in terms of imaging method, detection sensitivity, and noise resistance, the drawbacks of sampling time consumption make it unable to significantly replace and improve the performance of traditional imaging.[4–7] Therefore, reducing the sampling time consumption is one of the key problems in scientific research and the application of GI. In essence, a reduction in the sampling time consumption in GI can be achieved by reducing the number of light field coding required for high-quality imaging.

Finding ways to significantly reduce the measurement time and improve the imaging quality from less light field coding has become a hot spot of research. Common optical field encoding methods include random speckle,[2] Hadamard basis,[8] and Fourier basis matrix.[9,10] A large amount of research has shown that Hadamard basis (binary) and Fourier basis (grayscale) matrices with orthogonal properties exhibit better imaging performance than nonorthogonal random speckle matrices. Compact spatial light field modulation devices include liquid crystal spatial light field modulators and digital micro-mirror devices (DMD), etc. Among them, DMD has a modulation rate of up to 22 kHz under binary modulation and has significant advantages in refresh speed compared with other compact spatial light modulation devices. Therefore, selecting the Hadamard basis matrix and DMD for high-quality undersampling GI research is a better method.

The beginning of Hadamard 'Russian doll' sequence optimization work[11] made it possible to improve the performance of GI. By ordering Hadamard even from small to large, multiresolution progressive imaging can be realized,[12] and the measurement times of GI in the field of target recognition and other multiresolution imaging requirements can be reduced. An effective Hadamard basis ordering method for single-pixel imaging (SPI) based on generalized two-dimensional orthogonal bases,[13] which can be traversed in a zigzag fashion to order basis vectors from highest to lowest importance, allows the reconstruction of images at very low sampling rates. In the positive pattern-based Hadamard

†Corresponding author. E-mail: zhoucheng91210@163.com
‡Corresponding author. E-mail: qinhongwu@ccu.edu.cn
§Corresponding author. E-mail: ccdxslj@ccu.edu.cn

© 2024 Chinese Physical Society and IOP Publishing Ltd

SPI method,[14] the complementary strengths between the positive and negative modes are leveraged, successfully reducing the number of required measurements by half. Additionally, by combining a differential measurement strategy with ghost imaging theory, this technique can achieve high-quality imaging results even in noisy environments. To improve the imaging quality and practicability of the method, researchers have proposed an interconnection between bucket-shaped signals derived from the actual modulation of the standard Hadamard basis and their corresponding synchronous transformation modes.[15] Employing the conventional GI algorithm enables the reconstruction of images with superior quality. In terms of efficiency, the proposal of a method that uses the maximum projection algorithm to restructure Hadamard masks[16] for imaging has paved the way for achieving efficient and rapid image reconstruction. In recent years, a large number of optimization sequences and methods that can greatly improve the image quality under undersampling conditions have been proposed, such as Db2 wavelet,[17] Coiflet wavelet order,[18] Haar wavelet/dual domain,[19] 4-connected-region,[20] origami,[21] and others.[22–25] In addition, a ghost imaging scheme based on the mixed transformation method of the Hadamard matrix, discrete cosine matrix, and Haar matrix has been proposed,[26] which can easily reconstruct image information. Subsequently, there were also combinations of cake cutting sequences and compressed sensing methods,[27] as well as total variation and total wavelet transformed coefficients in ascending order optimization combined with deep learning methods.[28–30] These methods are processed by Hadamard sequence optimization or based on its sequence optimization. Although the imaging performance has been greatly improved, the implementation complexity of these methods has increased.

In this study, another non-optimized Hadamard matrix was switched to improve the quality of the undersampling imaging. Based on the aliasing characteristics of image reconstruction information under the condition of an undersampled natural-order Hadamard matrix (i.e., the lower the sampling times, the higher the aliasing degree), combined with deep learning, a high-quality ghost imaging method based on an undersampled natural-order Hadamard matrix is proposed. This method achieves image information restoration under various levels of aliasing and has great application potential and value for extremely low measurement times and data compression.

2. Methods

In the GI system, a light modulator projects the modulated light field onto an object with a reflection coefficient $O(x,y)$. The total reflected signals are collected using a bucket detector. The mth light field and bucket signal are represented by $I^{(m)}(x,y)$ and $B^{(m)}$, respectively. The reflected coefficient can be obtained by computing the correlation between $I^{(m)}(x,y)$ and $B^{(m)}$

$$O_{\mathrm{GI}}(x,y) = \frac{1}{M}\sum_{m=1}^{M}\left[\left(B^{(m)} - \left\langle B^{(m)}\right\rangle\right) \times \left(I^{(m)}(x,y) - \left\langle I^{(m)}(x,y)\right\rangle\right)\right], \tag{1}$$

where

$$\left\langle B^{(m)}\right\rangle = \frac{1}{M}\sum\nolimits_{m=1}^{M} B^{(m)},$$
$$\left\langle I^{(m)}(x,y)\right\rangle = \frac{1}{M}\sum\nolimits_{m=1}^{M} I^{(m)}(x,y).$$

Ghost imaging based on the natural-order Hadamard matrix can obtain nearly perfect image quality in full sampling, whereas overlapping image information will appear in undersampling. If the real information of the image can be extracted from the overlapping image, ghost imaging can be realized quickly using the undersampled natural-order Hadamard matrix. To address the issue of image overlap in the imaging results with an undersampling rate, we designed a U-shaped neural network. The network architecture is shown in Fig. 1. This network was derived from the U-Net proposed by Olaf Ronneberger *et al.* in 2015,[31] originally employed for image segmentation tasks in the medical field but applicable to image reconstruction tasks as well.[32] Adding a self-attention mechanism after each downsampling step in U-Net enhances the network's focus on crucial regions and features within the input image. This enhancement aids the network in capturing global features more effectively while maintaining and reconstructing detailed information, thereby improving the overall image reconstruction. The adaptability of this network transcends its initial medical applications, demonstrating its potential effectiveness in diverse imaging scenarios, particularly in the realm of image reconstruction from constrained sampling data.

The network is mainly composed of an encoder (downsampling), decoder (upsampling), intermediate skip connection, and self-attention mechanism after each downsampling. The encoder gradually decreases the spatial resolution through four downsamplings while increasing the number of feature channels to extract abstract features. Each downsampling module consists of a layer of convolution operation and a max pool for image feature extraction. The convolution operation comprises a 3×3 convolution layer, batch normalization (BN) layer, and activation layer using the ReLU function. Each layer performs two consecutive convolution operations, regardless of whether it is a part of the downsampling or upsampling process. The decoder is similar to the encoder in recovering picture information through four upsampling operations involving repeated steps of bilinear interpolation, inverse convolution, feature splicing, and two convolution operations. The convolutional layers employed in the upsampling

process comprised a 3×3 convolution layer and a 1×1 convolution layer. A notable feature of U-Net is the use of skip connections, which link the feature maps from the downsampling stage to their corresponding maps in the upsampling stage. This connection aids the network in recovering lost detailed information. Each downsampling process in the network's encoder facilitates learning of the global features of the input image. To further enhance the network's focus on crucial regions and features in the input image, a self-attention module was introduced after each downsampling step.

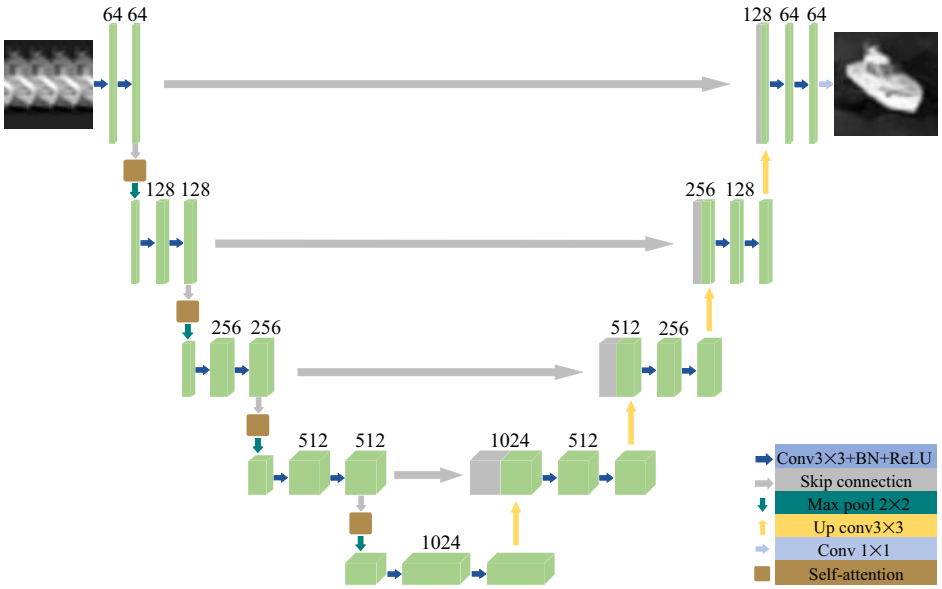


Fig. 1. Network model architecture. The self-attention module was added to the original U-Net.

We used the self-attention mechanism to process the image after each downsampling step, enabling the model to learn the dependencies between different regions within the image. This approach highlights key features and reduces interference from irrelevant information. This mechanism achieves image localization by dynamically adjusting region weights, thereby capturing both global and local information. It generates a feature map of the same size as the input image, which identifies regions associated with location and labels categories through a global computational approach. This mechanism operates on feature mapping obtained through convolution. It first computes the dot product between query ($\boldsymbol{Q}$) and key ($\boldsymbol{K}$), and then scales it by dividing by $\sqrt{d_k}$ to obtain the attention score. Next, SoftMax classification was performed to obtain the weights for each position. Each position had a value of $\boldsymbol{V}$. Finally, the output was computed from the matrices $\boldsymbol{Q}$, $\boldsymbol{K}$, and $\boldsymbol{V}$:

$$\text{Attention}\left(\boldsymbol{Q},\boldsymbol{K},\boldsymbol{V}\right)=\text{SoftMax}\left(\frac{\boldsymbol{Q}\boldsymbol{K}^{\text{T}}}{\sqrt{d_k}}\right)\boldsymbol{V}, \tag{2}$$

where $\boldsymbol{K}^{\text{T}}$ is the column number of the matrices $\boldsymbol{Q}$ and $\boldsymbol{K}$.

It is well known that network training requires a large number of ghost images as training datasets to obtain better reconstruction results. To acquire this training dataset, we designed a ghost imaging simulation system. By acquiring the necessary dataset from the image database as input for the system, a significant number of ghost imaging-simulated images can be rapidly generated. This not only diminishes the complexity of network training but also significantly saves time and cost.

Finally, we need to choose a suitable loss function for network training. The loss functions for the reconstructed image task include MSE loss, SSIM loss, perceptual loss, and others. In this study, the chosen loss function for network training was MSE loss, defined as

$$\text{MSE}=\frac{1}{N}\sum_{i=1}^{N}\left(y_i-h\left(x_i\right)\right)^2, \tag{3}$$

where y_i is the true value of the ith sample, $h(x_i)$ is the predicted value of the ith sample, and N is the number of samples. The smaller the value of this loss function, the closer the prediction result of the model to the true value. This not only met our task requirements but also reduced the computation of the network and improved the network efficiency. Our network model used the Adam optimizer to update the neural network parameters based on the gradient information, thereby minimizing the loss function. The initial learning rate lr of Adam was 0.001. All tasks were performed in a workstation (@Intel-Xeon CPU and 1×@NVIDIA GeForce RTX 3090 GPU).

3. Results

The goal of this study was to demonstrate the effectiveness of the proposed method in resolving the issue of overlapping imaging results in CGI when undersampling is per-

formed, thus addressing the inability of CGI to achieve high-quality results within a short period of time and meet the requirements of rapid imaging applications. We used a natural-order Hadamard matrix as the spatial light field and conducted CGI numerical simulations at various sampling times.

3.1. Numerical simulation results

To demonstrate the validity and comprehensiveness of the method, we used the MNIST dataset[33] and ship dataset from CIFAR-10.[34] These datasets were converted to grayscale and resized to 64×64 pixels as target objects. From these, 3000 images were selected as the training set and 100 images as the test set. A CGI simulation system with a single light field size of 64×64 pixels, composed of natural-order Hadamard matrices, was employed. The target object was input into the CGI simulation system for undersampling to obtain an overlapping image. This aliasing occurs because, when undersampling is performed, the natural order reconstructs the image with a strong aliasing effect, resulting in multiple copies of the true image. Subsequently, network training was conducted to obtain the reconstruction results. To objectively evaluate the performance of the method, we used the peak signal to noise ratio (PSNR) and structural similarity (SSIM) as the evaluation metrics. PSNR is defined as

$$\mathrm{PSNR} = 10 \times \log_{10}\left[\frac{\max \mathrm{Val}^2}{\mathrm{MSE}}\right], \tag{4}$$

where $\mathrm{MSE} = \frac{1}{r\times c}\sum_{i=1}^{r}\sum_{j=1}^{c}\left[u(i,j)-x(i,j)\right]^2$, and max Val is the maximum possible pixel value of the image. SSIM measures the similarity between the reconstructed and original images in terms of brightness, contrast, and structure. This is defined as

$$\mathrm{SSIM} = \frac{(2\mu_x\mu_y + C_1)(2\sigma_{xy} + C_2)}{(\mu_x^2 + \mu_y^2 + C_1)(\sigma_x^2 + \sigma_y^2 + C_2)}, \tag{5}$$

where x is the original image; y is the reconstructed image; μ_x and μ_y denote the mean value of x and y, respectively; σ_x^2 and σ_y^2 denote the variances of x and y, respectively; σ_{xy} denotes the covariance of x and y; and C_1 and C_2 are constants.

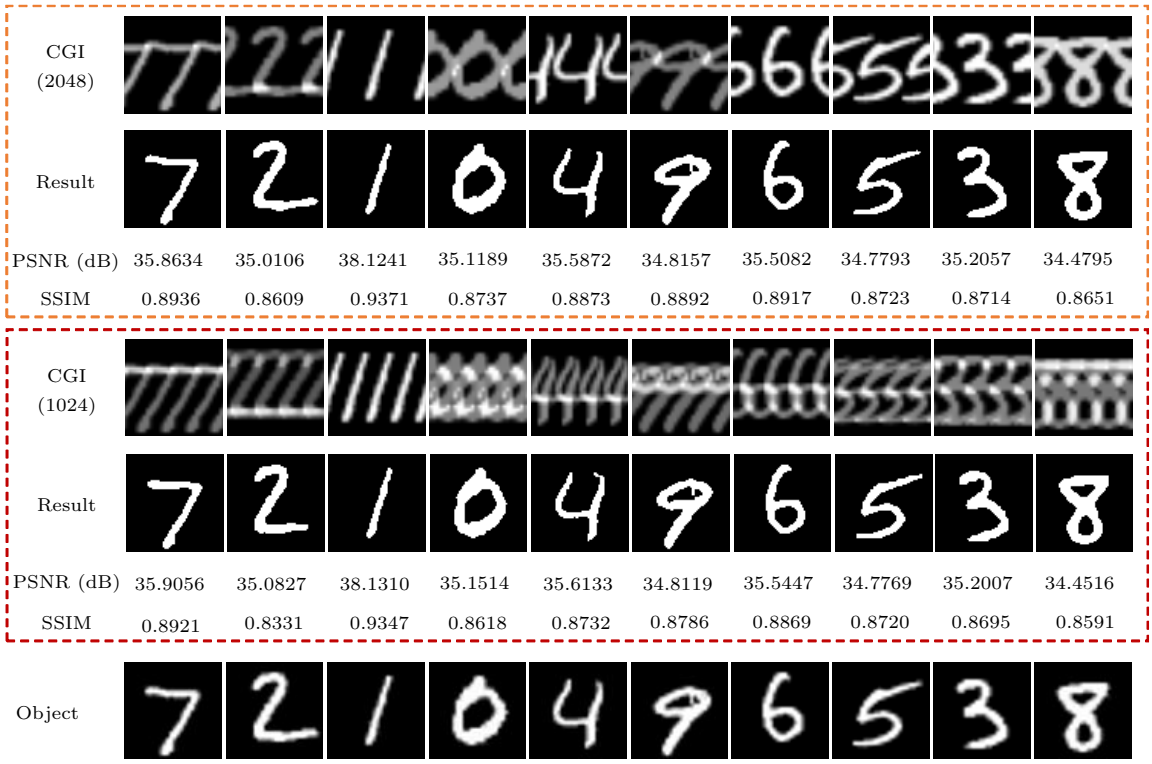


Fig. 2. Numerical simulation results of CGI deep learning at 2048 (50%) and 1024 (25%) sampling times, simultaneously showing the digital target image and numerical values of PSNR and SSIM. First row in the orange box: CGI simulation results at 2048 (50%) sampling times; second row: reconstruction results obtained using deep learning. First row in the red box: CGI simulation results at 1024 (25%) sampling times; second row: reconstruction results obtained using deep learning; last row: original image of the target.

First, we used the MNIST dataset as the target image. It took approximately 50 minutes to train 300 epochs through the network and approximately 0.011 s to reconstruct the image. As depicted in Fig. 2, the last row in the entire result map represents the target image, whereas the remaining portions are divided into two parts: the upper orange box (2048 times sampling; sampling rate of 50%) and the lower red box (1024 times sampling; sampling rate of 25%). In the orange box, the first row was obtained as an overlapping image at 2048 (50%) sampling times in the CGI simulation system. The obtained overlapping image was brought into our deep learning network for training and then tested to obtain the reconstructed

result, as shown in the second row in the orange box of Fig. 2. In the red box, the first row is the overlapped image obtained by CGI at 1024 (25%) sampling times. It is evident that the overlap is significantly greater than that of the imaging results obtained at 2048 (50%) sampling times. The second row in the red box of Fig. 2 displays the reconstructed image after processing through the deep learning network. We can see that the results reconstructed using the proposed method are very similar to the target image at both 2048 (50%) and 1024 (25%) sampling times. PSNR was approximately 35 dB, whereas the SSIM values were approximately 0.87, with the highest value reaching 0.9371. This proves the effectiveness of the proposed method.

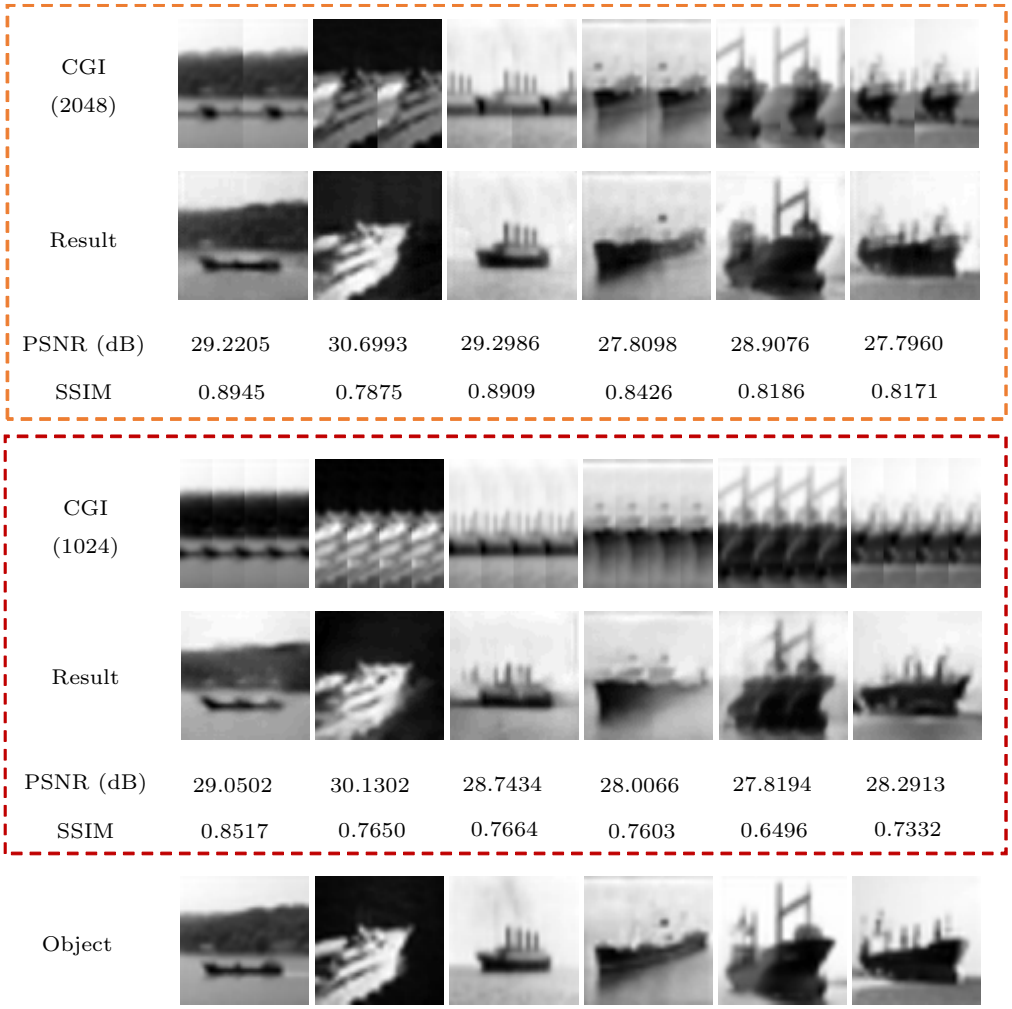


Fig. 3. Numerical simulation results of CGI deep learning at 2048 (50%) and 1024 (25%) sampling times, simultaneously showing the ship target image and numerical values of PSNR and SSIM. First row in the orange box: CGI simulation results at 2048 (50%) sampling times; second row: reconstruction results obtained using deep learning. First row in the red box: CGI simulation results at 1024 (25%) sampling times; second row: reconstruction results obtained using deep learning; last row: original image of the target.

To demonstrate the practicality of the proposed method, we selected the ship dataset within CIFAR-10 as the target image, which is close to practical applications. It took approximately 80 minutes to train 300 epochs through the network and approximately 0.048 s to reconstruct the image. The first rows in the orange and red boxes of Fig. 3 show the overlapped images obtained by CGI at 2048 (50%) and 1024 (25%) sampling times, respectively. As can be seen from the figure, only a few images show that the target image is a ship from some local features, and most of the images cannot identify the target image as a ship. The image of the ship contains more detailed information than the digital image, which is more complex, making it more difficult to accurately obtain the overall information of the ship. We trained the network with overlapping images at 2048 (50%) and 1024 (25%) sampling times of the ship as the target image and finally obtained the reconstruction results, which are shown in the second rows in the orange and red boxes of Fig. 3, respectively. From the reconstruction results, it can be seen that the overlapping problem of the image was effectively solved, and the overall contour and most of the information features of the ship were effectively recovered. Both the PSNR and SSIM values demonstrated good performance. Experiments proved that the proposed method is effective for complex target images. How-

ever, in cases where the picture information is highly complex and the sampling times are low, the reconstruction results may still exhibit a local overlap. For example, in the fourth image of the second row in the red box of Fig. 3 (reconstruction results at 1024 (25%) sampling times), it can be seen that there is an overlap between the sails of the ship and the flagpole, which lacks some detailed features of the image. These problems are solved using the training dataset and the deep learning network model, and we will improve and refine these aspects in the future.

3.2. Experimental results

To verify that the method can realistically meet the requirement of obtaining high-quality imaging results during undersampling, we conducted practical experiments. As illustrated in Fig. 4, the experimental system consisted of a light source, target object, focusing lens, imaging lens, DMD, and a single-phase element detector. The DMD was a 1024×768 micro-mirror array device. Each micro-mirror can switch in the ±12° directions, corresponding to 1 and 0. The modulation frequency of the DMD can load binary spatial light field patterns at a speed of 22k patterns per second. Under ambient illumination (Thorlabs MCWHLP1 cold white LED), the projected light illuminated on the target object was directed through the lens to the DMD (Vialux V7000) for light field modulation. The echo signal reflected on the DMD was focused on a single-pixel detector (Thorlabs, PDA100A2) through the lens. The target object was a digital mask model with a diameter of 25.8 mm ('Object' in Fig. 4). It was located approximately 24.2 cm away from the DMD, and the DMD was approximately 26.4 cm away from the single-pixel detector.

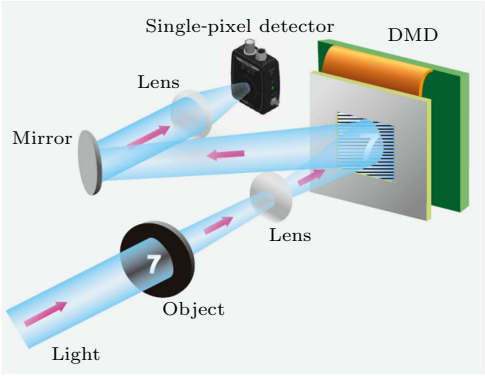


Fig. 4. Experimental system diagram of computational ghost imaging.

We used a 3D printer to produce skeletonized versions of numbers 4 and 7, as well as a laser engraver to engrave skeletonized versions of numbers 2, 1, and 7 onto an acrylic plate as experimental objects, as shown in the last row of Fig. 5. The digital target objects were detected using a CGI system consisting of a natural-order Hadamard matrix with a single light field size of 64×64 pixels. The first rows in the orange and red boxes of Fig. 5 show the results of the CGI experiment at 2048 (50%) and 1024 (25%) sampling times, respectively. It can be seen that the image results of the CGI experiments have the same effect as the overlapping images obtained from the numerical simulation. Finally, the experimental results were introduced into the deep learning model to obtain the reconstruction results, and the reconstruction time was approximately 0.013 s. The second rows in the orange and red boxes of Fig. 5 display the reconstruction results of the deep learning network at 2048 (50%) and 1024 (25%) sampling times, respectively. It was proved that the method can effectively remove image overlapping at undersampling and achieve high-quality reconstruction results.

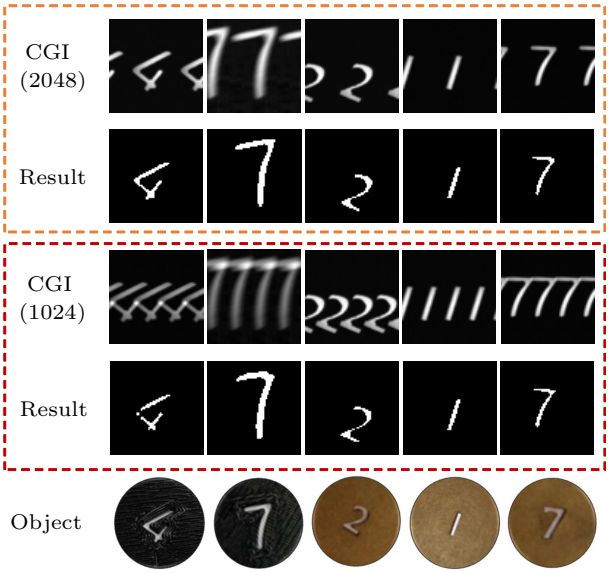


Fig. 5. Experimental results of CGI deep learning at 2048 (50%) and 1024 (25%) sampling times. First row in the orange box: CGI experimental results at 2048 (50%) sampling times; second row: reconstruction results obtained using deep learning. First row in the red box: CGI experimental results at 1024 (25%) sampling times; second row: reconstruction results obtained using deep learning; last row: target object image.

4. Discussion

To further validate the performance of the proposed approach, we obtained aliased images at 512 (12.5%) and 256 (6.25%) sampling times after passing them through a CGI simulation system consisting of natural-order Hadamard matrices. The results are depicted in Fig. 6. The first rows in the orange and red boxes represent the overlapping images obtained by CGI at 512 (12.5%) and 256 (6.25%) sampling times, respectively. The second row corresponds to the reconstruction outcomes under the sampling times, with the last row being the target image. As shown in Fig. 6, the fewer the sampling times, the greater the degree of overlap of the images. The performance superiority of this method can be confirmed by the reconstruction results and the PSNR and SSIM values.

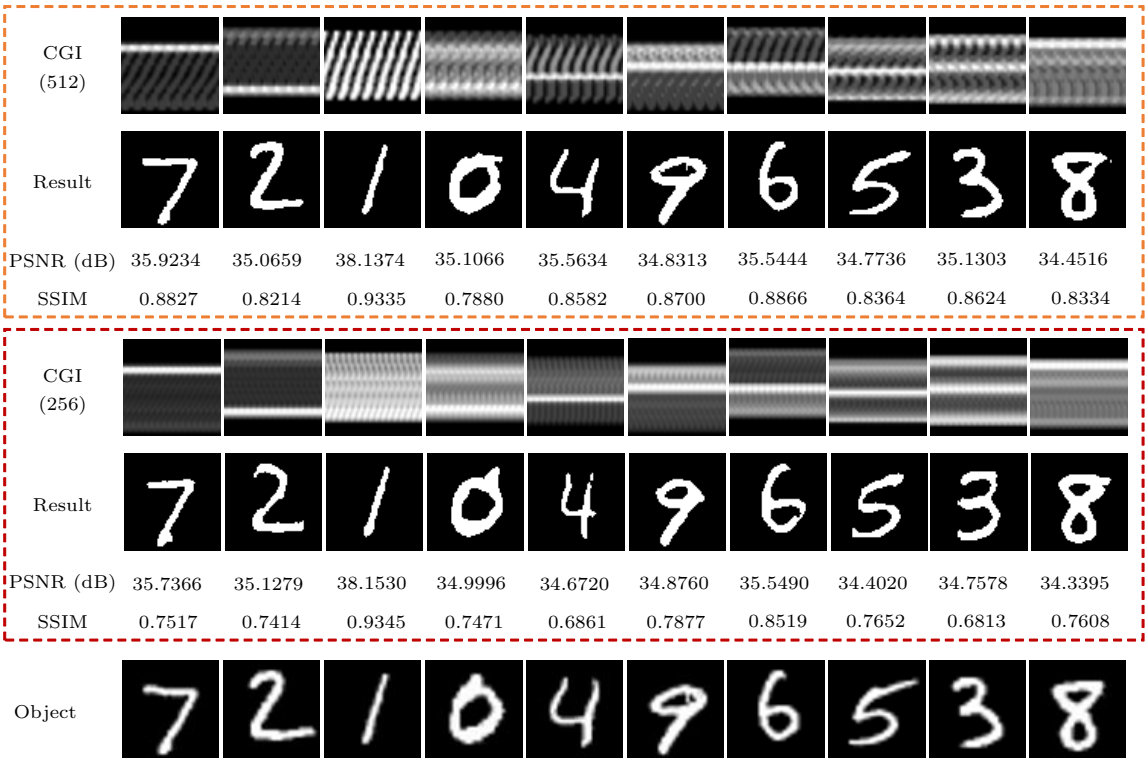


Fig. 6. Numerical simulation results of CGI deep learning sampled at 512 (12.5%) and 256 (6.25%) times, simultaneously showing the digital target image and the PSNR and SSIM numerical values. First row in the orange box: CGI simulation results at 512 (12.5%) sampling times; second row: reconstruction results obtained using deep learning. First row in the red box: CGI simulation results at 256 (6.25%) sampling times; second row: reconstruction results obtained using deep learning; last row: original image of the target.

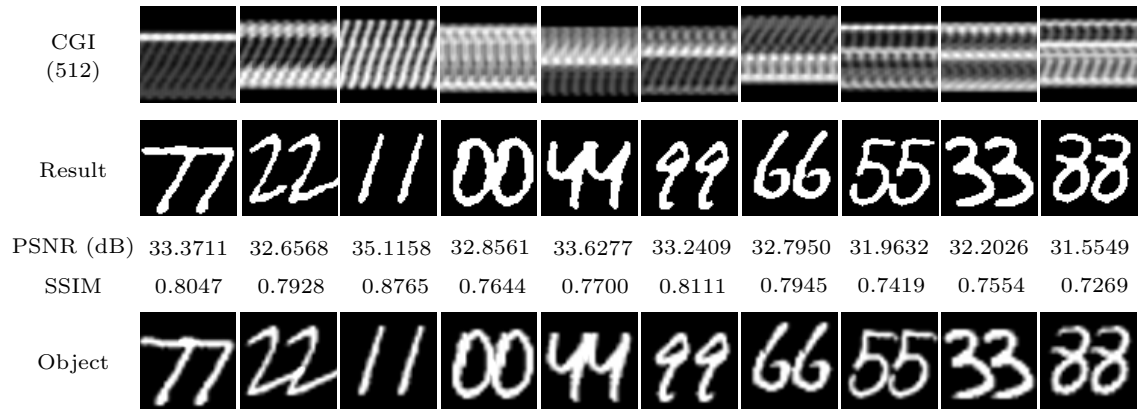


Fig. 7. Numerical simulation results of periodic array objects.

Simultaneously, we processed the MNIST dataset by arranging the numbers in the image in a periodic array from a single numerical target in the original plot to multiple numerical targets that are homogeneous and identical, as shown in the last row of Fig. 7. The processed images were acquired when ghost imaging was performed at 512 (12.5%) sampling times to obtain overlapping images, as shown in the first row of Fig. 7. Finally, the acquired aliased images were reconstructed using the deep learning method in this study, and the results are shown in the second row of Fig. 7. From the reconstruction results and the PSNR and SSIM values, it can be verified that the method performs well in periodic array objects.

The proposed method can be applied to several fields of ghost imaging. In the medical field, x-ray ghost imaging combined with the deep learning network in this study can be used for fluoroscopy and radiography of teeth to help doctors obtain images of the internal structure of teeth. Through these images, doctors can accurately diagnose dental diseases, such as dental caries, pulpitis, and periodontitis. They can also clearly see the internal structure and defects of the teeth so that they can better select implants and restorative materials, as well as improve the success rate and effect of the surgery. As shown in Fig. 8, the last row is a single tooth intercepted from the DEN-TEX dataset[35] as the target image, the first row is the overlapped image obtained using CGI, and the second row is

the reconstruction result of the deep learning method used in this study. In conclusion, this method has a wide range of applications in the field of medical dentistry, which can help doctors diagnose and treat dental diseases more accurately, as well as improve the treatment effect and quality of life of patients.

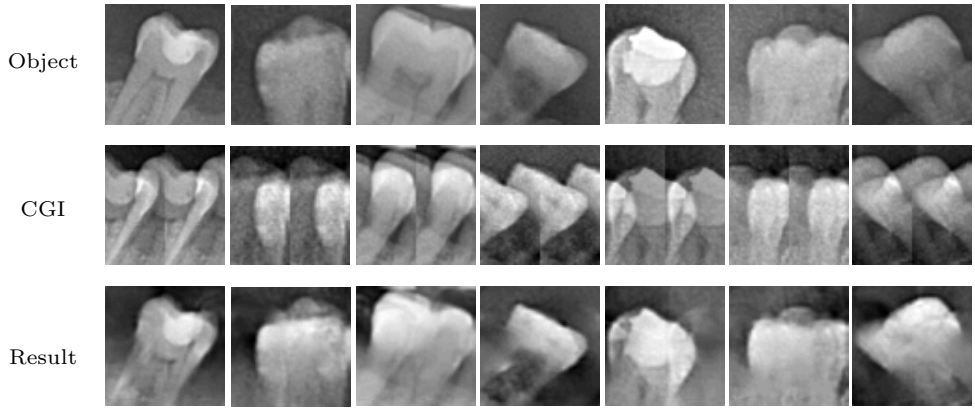


Fig. 8. Numerical simulation results of x-ray images of teeth.

5. Conclusion

In this study, we propose and demonstrate a novel ghost imaging method that utilizes undersampled natural-order Hadamard light fields in conjunction with deep learning techniques. We conducted numerical simulations and experimental verifications on the property of obtaining aliased images through ghost imaging under undersampling conditions of a natural-order Hadamard light field using binary digital and grayscale ship data with $1/2$ and $1/4$ sampling. By processing the aliasing information obtained from undersampling through deep learning, high-quality real-time imaging can be achieved.

Acknowledgements

Project supported by the Science and Technology Development Plan Project of Jilin Province, China (Grant No. 20220204134YY), the National Natural Science Foundation of China (Grant No. 62301140), Project of the Education Department of Jilin Province (Grant Nos. JJKH20231292KJ and JJKH20240242KJ), Program for Science and Technology Development of Changchun City (Grant No. 23YQ11), Innovation and Entrepreneurship Talent Funding Project of Jilin Province (Grant No. 2023RY17), and the Project of Jilin Provincial Development and Reform Commission (Grant No. 2023C042-4).

References

[1] Shapiro J H 2008 *Phys. Rev. A* **78** 061802
[2] Bromberg Y, Katz O and Silberberg Y 2009 *Phys. Rev. A* **79** 053840
[3] Liu J F, Dong Y, Wang L and Zhao S M 2023 *Chin. Phys. B* **32** 074202
[4] Edgar M P, Gibson G M and Padgett M J 2019 *Nat. Photonics* **13** 13
[5] Gibson G M, Johnson S D and Padgett M J 2020 *Opt. Express* **28** 28190
[6] Fu Q, Bai Y, Tan W, Huang X, Nan S and Fu X 2023 *Chin. Phys. B* **32** 064203
[7] Liu Z Q, Bai Y F, Zou X P F, Zhou L Y, Fu Q and Fu X Q 2023 *Chin. Phys. B* **32** 034210
[8] Wang L and Zhao S 2016 *Photon. Res.* **4** 240
[9] Zhang Z, Ma X and Zhong J 2015 *Nat. Commun.* **6** 6225
[10] Qiu Z, Zhang Z and Zhong J 2020 *Opt. Lasers Eng.* **134** 106301
[11] Sun M J, Meng L T, Edgar M P, Padgett M J and Radwell N 2017 *Sci. Rep.* **7** 3464
[12] Zhou C, Tian T, Gao C, Gong W and Song L 2019 *J. Opt.* **21** 055702
[13] López-García L, Cruz-Santos W, García-Arellano A, Filio-Aguilar P, Cisneros-Martínez J A and Ramos-García R 2022 *Opt. Express* **30** 13714
[14] Sun R, Long J, Ding Y, Kuang J and Xi J 2023 *In Photonics MDPI* **10** 395
[15] Bie S H, Wang C H, Lv R B, Bao Q Q, Fu Q, Meng S Y and Chen X H 2023 *Chin. Phys. B* **32** 128702
[16] Zhang H P, Du K, Zhao C Z, Tang J, Si S Y, Jia W H, Xue L and Li Z L 2023 *Sci. Rep.* **13** 22702
[17] Yu X, Yang F, Gao B, Ran J and Huang X 2020 *IEEE Access* **8** 55773
[18] Wu H, Zhao G, He C, Cheng L and Luo S 2022 *Phys. Rev. A* **106** 053522
[19] Yu Z, Gao C, Wang X Q, Zhao H and Yao Z H 2022 *Opt. Laser Technol.* **155** 108413
[20] Wu H, Zhao G, Wang R, Xiao H, Wang D, Liang J, Cheng L and Liang R 2020 *Opt. Lasers Eng.* **132** 106105
[21] Yu W K and Liu Y M 2019 *Sensors* **19** 5135
[22] Huang H and Han Z 2024 *Opt. Commun.* **552** 130096
[23] Guo H, Wang L and Zhao S M 2022 *Chin. Phys. B* **31** 084201
[24] Li M F, Yan L, Yang R and Liu Y X 2019 *Acta Phys. Sin.* **68** 064202 (in Chinese)
[25] Zhou C, Liu X, Feng Y S, Li X W, Wang G C, Sun H Z, Huang H Y and Song L J 2022 *Opt. Lasers Eng.* **156** 107101
[26] Zhao Y N, Chen L S, Chen L Y, Kong L, Wang C, Ren C, Zhang S H and Cao D Z 2024 *arXiv.eess.IV* arXiv: 2405.03729
[27] Yu W K 2019 *Sensors* **19** 4122
[28] Huang Y Y, Ou-Yang C, Fang K, Dong Y F, Zhang J, Chen L M and Wu L A 2021 *Chin. Phys. B* **30** 064202
[29] Zhang H, Xia Y and Duan D 2021 *Chin. Phys. B* **30** 124209
[30] Li Y and Duan D 2023 *Chin. Phys. B* **32** 104203
[31] Ronneberger O, Fischer P and Brox T 2015 *In Medical image computing and computer-assisted intervention–MICCAI* 2015*:* 18*th international conference*, Munich, Germany, October 5–9, 2015, proceedings, part III 18 pp. 234–241
[32] Jin K H, McCann M T, Froustey E and Unser M 2017 *IEEE Trans. Image Process.* **26** 4509
[33] LeCun Y, Bottou L, Bengio Y and Haffner P 1998 *Proc. IEEE* **86** 2278
[34] Krizhevsky A and Hinton G 2009 *Tech. Rep.* 001
[35] Hamamci I E, Er S, Simsar E, Sekuboyina A, Gundogar M, Stadlinger B, Mehl A and Menze B 2023 arXiv:2303.06500